Mesoporous Ceria and Ceria-Praseodymia as High Surface Area Supports for Pd-based Catalysts with Enhanced Methane Oxidation Activity

ChemCatChem

Research Article
doi.org/10.1002/cctc.202301359

Chemistry Europe
European Chemical Societies Publishing

www.chemcatchem.org

Hot Paper

Mesoporous Ceria and Ceria-Praseodymia as High Surface Area Supports for Pd-based Catalysts with Enhanced Methane Oxidation Activity

Sabrina Ballauri,[a] Enrico Sartoretti,*[a] Micaela Castellino,[a] Marco Armandi,[a] Marco Piumetti,[a] Debora Fino,[a] Nunzio Russo,[a] and Samir Bensaid*[a]

In recent years, Pd/CeO_2 materials have proven to be effective catalysts for the total oxidation of methane. In this work, three different synthesis routes were used to prepare high specific surface area supports, consisting of pure CeO_2 and 10 at% Pr-doped ceria (Ce90Pr10). Nano-structured spheres were obtained with a microwave-assisted synthesis, dumbbell-like particles were produced through a urea-based hydrothermal method, and ordered mesoporous oxides were prepared by using SBA-15 as hard-template. The six materials were then impregnated with 2 wt% Pd, calcined at 500 °C, and comprehensively characterized. All the samples retained their high surface area after impregnation (75–110 $m^2 g^{-1}$), allowing a good dispersion of palladium. No significant structural or morphological differences were observed upon Pr doping, but a higher Pd oxidation state was induced by Pr-doped supports. However, all Pd/CeO_2 and Pd/Ce90Pr10 catalysts exhibited similar activity for dry methane oxidation below 500 °C, regardless of the synthesis technique and of the Pr presence: they all achieved almost complete CH_4 oxidation at 400 °C, showing a really remarkable improvement with respect to analogous low surface area supports. A promoting role of Pr was instead noticed in wet conditions, thanks to its ability to counteract water-induced deactivation phenomena.

Introduction

The employment of less impacting energy sources has become essential having regard to the serious climate and environmental problems that the world is facing nowadays. As a direct consequence, the use of cleaner fossil fuels (such as natural gas and methane) turns out to be imperative to reduce the emissions of pollutants into the atmosphere. Methane is indeed characterized by a higher fuel efficiency and lower carbon emission with respect to other heavy fossil fuels.[1,2] Despite these favorable features, unburned methane emissions represent a critical issue looking at the higher Global Warming Potential of CH_4 with respect to that of CO_2. Furthermore, the atmospheric methane concentration is exponentially increasing compared to pre-industrial levels.[3–5]

Currently, Pd-based catalysts are considered the best choice for reducing the methane emissions through its complete oxidation, considering their high activity at relatively low temperature.[6–10] Although these materials have already been extensively studied, further efforts are needed to limit the loss of activity around 700–800 °C due to the PdO-Pd transition and the detrimental effects of water.[11–14] In this context, the Pd deposition on Ce–Pr supports has been investigated over the past few years, obtaining materials with a higher catalytic activity with respect to Pd/CeO_2, a better stability of the PdO species in the high temperature range, and an interesting behavior in the presence of water.[15,16] However, these materials were characterized by very low surface area values, while an increase in this parameter can be expected to considerably improve the catalytic performance of these catalysts.[17,18]

Hence, in this study the deposition of palladium species on high-surface area Ce–Pr catalysts was performed. Mesoporous CeO_2 and Ce90Pr10 (with 10 at% Pr doping) supports were prepared by using three different synthesis procedures (i.e. synthesis in a microwave digestor, hydrothermal synthesis at low temperature, and synthesis with the use of a hard template) and then impregnated with a palladium solution. Throughout this work, Pd/CeO_2 and Pd/Ce90Pr10 catalysts were comprehensively characterized by employing different techniques and tested for the methane oxidation reaction in both dry (i.e. in the absence of water) and wet (i.e. in the presence of water) conditions. The long-term stability of these materials in the presence of water was also investigated.

[a] S. Ballauri, Dr. E. Sartoretti, Dr. M. Castellino, Prof. M. Armandi, Prof. M. Piumetti, Prof. D. Fino, Prof. N. Russo, Prof. S. Bensaid
Department of Applied Science and Technology
Politecnico di Torino
Corso Duca degli Abruzzi, 24, 10129 Turin (Italy)
E-mail: enrico.sartoretti@polito.it
samir.bensaid@polito.it

Supporting information for this article is available on the WWW under https://doi.org/10.1002/cctc.202301359

Results and Discussion

Characterization of the powdered catalysts

Table 1 shows the main structural properties of the catalysts along with their actual composition. The surface area of the catalysts (S_{BET}) is quite high and ranges from 76 to 84 $m^2 g^{-1}$ for Ce–Pr spheres and dumbbells, while a greater value was observed for the two catalysts obtained using SBA-15 as a hard template. The latter materials were indeed characterized by a BET surface area of around 110 $m^2 g^{-1}$ and such a result is in line with samples obtained in the literature through a similar synthesis technique.[19,20] Comparing Tables 1 and S1 shows that the surface area values of bare supports and Pd-based materials are very close to each other. Overall, a very slight reduction in this parameter was observed after the palladium impregnation and the second calcination at 500 °C. As to the catalysts prepared without using any template (spheres and dumbbells), both catalytic carriers and Pd-materials were distinguished by isotherms with shapes akin to type II of IUPAC classification, with type H3 hysteresis loop (Figures S1 and S2); the lower limit of the desorption branch was identified at the cavitation-inducted p/p^0 equal to 0.4.[21] In fact, these materials are characterized by an interparticle porosity, due to the self-assembly of particles. On the other hand, samples obtained by using SBA-15 as a hard template showed a type IV isotherm. In these materials, the hysteresis loop closed at higher p/p^0 value, hence the capillary condensation occurs in a narrow range of pressure corresponding to larger pore width. This fact is also confirmed by the pore volume values (V_P) presented in Table 1. Indeed, the samples synthesized with hard template method exhibited a significantly higher pore volume compared to the other catalysts.

Figures S3 and 1 illustrate the X-ray diffraction patterns of supports and Pd-containing materials, respectively. The presence of the (111), (200), (220), (311), (222), (400), (331) and (420) peaks proves the presence of the typical cubic fluorite structure of CeO_2 catalysts.[22–24] Moreover, considering that no peak splitting was observed within the patterns reported in Figure S3 and Figure 1, a solid solution between ceria and praseodymia was formed in the Ce90Pr10 samples.[25] This result was expected, considering the very close ionic radii of Ce^{4+}/Ce^{3+} and Pr^{4+}/Pr^{3+} ions ($Ce^{4+} = 0.97$ Å, $Ce^{3+} = 1.143$ Å, $Pr^{4+} = 0.96$ Å, $Pr^{3+} = 1.126$ Å).[26] Looking at the diffractograms of Pd-impregnated samples, displayed in Figure 1, peaks close to 33.8° and 40° were not observed. It means that neither PdO nor Pd are present in large domains in the catalytic structure[27] and a good dispersion of Pd was obtained.

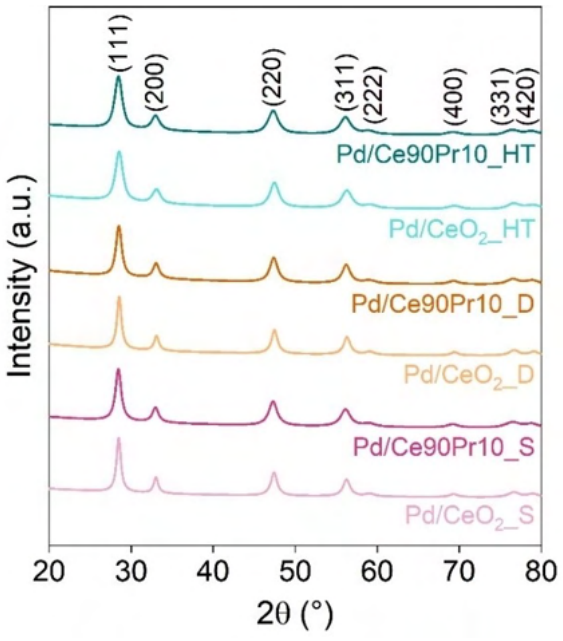

Figure 1. X-Ray diffraction patterns of Pd/CeO_2 and Pd/Ce90Pr10 catalysts.

The average crystallite size (D_C) of supports and Pd-based catalysts was evaluated by employing Scherrer's equation and the results are reported in Table 1 and S1. All the samples are distinguished by rather small crystallites with dimensions ranging from 7–7.3 nm for materials obtained by using SBA-15 as a hard template to 8.8–12.2 nm for materials obtained without using any template (spheres and dumbbells). As expected, samples characterized by a higher surface area exhibited smaller crystallites. Some variations from this trend may be related to the presence of a partial agglomeration phenomenon.[15,28] The average crystallite size remained almost unchanged by moving from the supports to the Pd-containing materials. In some cases, this parameter showed a slight increase due to the additional calcination treatment after the impregnation.

Table 1. Structural properties and actual composition of Pd/Ce–Pr catalysts.

Sample	S_{BET} ($m^2 g^{-1}$)[a]	V_P ($cm^3 g^{-1}$)	D_C (nm)[b]	Pd loading (wt %)[c]	Ce-to-Pr ratio[c]
Pd/CeO_2_S	79	0.03	12.1	1.7	–
Pd/Ce90Pr10_S	84	0.04	8.8	1.6	9.57
Pd/CeO_2_D	76	0.05	12.2	1.5	–
Pd/Ce90Pr10_D	76	0.05	9.3	1.4	9.02
Pd/CeO_2_HT	113	0.34	7.3	1.2	–
Pd/Ce90Pr10_HT	106	0.30	7.0	1.4	9.00

[a] Evaluated through the BET method. [b] Calculated by applying Scherrer's equation. [c] Obtained through ICP analysis.

The proper composition of the catalysts was checked by inductively coupled plasma-mass spectrometry (ICP-MS) analysis. According to Table 1, the percentage of palladium present in the catalysts turned out to be lower than the nominal value (2 wt%) for all the samples, ranging from 1.2 to 1.7 wt%. In addition, the Ce-to-Pr ratio, evaluated for Ce90Pr10 samples, complied well with the expected one.

The catalyst morphology was first studied through field emission scanning electron microscopy (FESEM) and the obtained images are reported in Figure 2 and 3. Figure 2a and Figure 2b show the FESEM micrographs of Pd/CeO_2_S and Pd/Ce90Pr10_S materials obtained without template reproducing the synthesis procedure described in.[29] However, as opposed to what is described in the reference paper, uniform spherical particles with a confined distribution were not present in the samples of this work. Indeed, larger spheres (1–3 μm) covered by smaller spherical particles (100–300 nm) were noticed (as shown in the lower-magnification image in Figure 3a). This difference is acceptable and could be attributed to the different experimental setups employed.

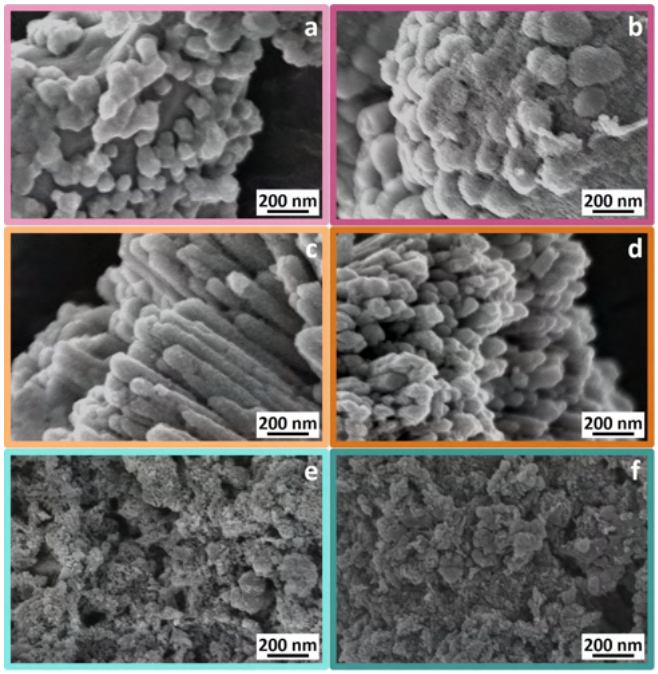

Figure 2. FESEM images of Pd/CeO_2_S (a), Pd/Ce90Pr10_S (b), Pd/CeO_2_D (c), Pd/Ce90Pr10_D (d), Pd/CeO_2_HT (e), Pd/Ce90Pr10_HT (f).

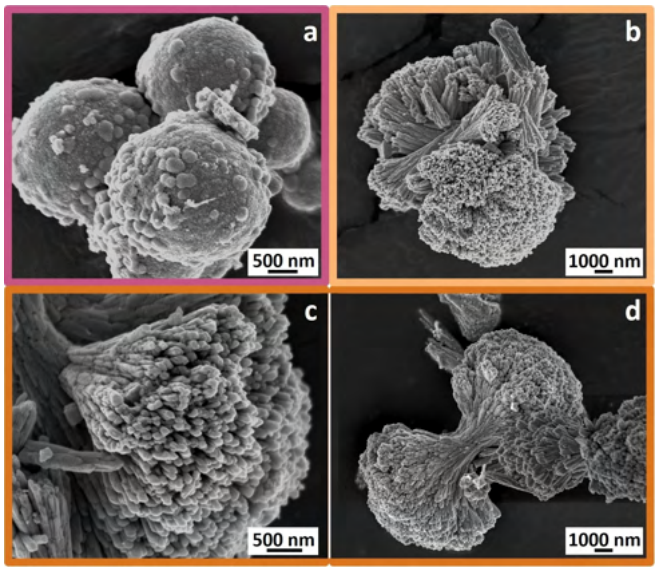

Figure 3. Additional FESEM images at lower magnification of Pd/Ce90Pr10_S (a), Pd/CeO_2_D (b) and Pd/Ce90Pr10_D (c,d).

Figure 2c and Figure 2d exhibit the FESEM micrographs of Pd/CeO_2_D and Pd/Ce90Pr10_D catalysts prepared without any template, following the procedure described in.[30] As per the latter, in the Pd/CeO_2_D sample, the presence of Ce^{3+} ions (from $Ce(NO_3)3\cdot6H_2O$) and urea in the synthesis solution leads to the formation of well-defined particles with a dumbbell-like shape. Throughout this work, it was possible to prove that this peculiar structure can be also achieved in doped ceria systems, in particular when adding 10 at% of praseodymium in the lattice of CeO_2. As a matter of fact, the dumbbell-like shape was also detected for the Pd/Ce90Pr10_D sample, as evident from the additional lower-magnification images provided in Figure 3.

Figure 2e and Figure 2f illustrate the FESEM micrographs of the Pd/CeO_2_HT and Pd/Ce90Pr10_HT samples synthesized by using SBA-15 as a hard template and following the preparation method described in.[31] Pd/CeO_2_HT and Pd/Ce90Pr10_HT were characterized by rather agglomerated particles, separated by interparticle voids. The same morphology was detected for the mesoporous ceria studied in,[32] proving the success of the synthesis method.

Subsequently, the morphology of the samples was further investigated through high resolution transmission electron microscopy (HRTEM), and the related images are reported in Figure 4. In the pure ceria catalysts (CeO_2_S, CeO_2_D and CeO_2_HT), lattice fringes typical of CeO_2(220) and CeO_2(111) domains were observed (interplanar distance of 0.191–0.195 and 0.309–0.318 nm, respectively).[33,34] As regards the praseodymium-containing catalysts, it is quite tough to differentiate the eventual presence of segregated ceria from segregated praseodymia domains by using this technique. Nevertheless, considering the marked similarity between the crystalline structures of cerium and praseodymium oxides,[35] as well as the absence of a peak-splitting phenomenon in the XRD patterns, the lattice lines observed in the Ce90Pr10 materials can be ascribed to CeO_2-PrO_x mixed particles. Therefore, lattice fringes with interplanar distances ranging from 0.305 to 0.311 nm were assigned to CeO_2-PrO_x(111) domains.

As far as palladium is concerned, it is very difficult to spot the presence of well-defined isolated noble metal particles on the Ce–Pr supports due to the employed impregnation technique (common incipient wetness impregnation). However, some small crystalline domains related to Pd species were detected in various areas of the materials. In more detail, lattice fringes characterized by interplanar distance of 0.264–0.266 nm were observed in all the Pd/Ce–Pr catalysts and assigned to the presence of PdO(002) planes.[36]

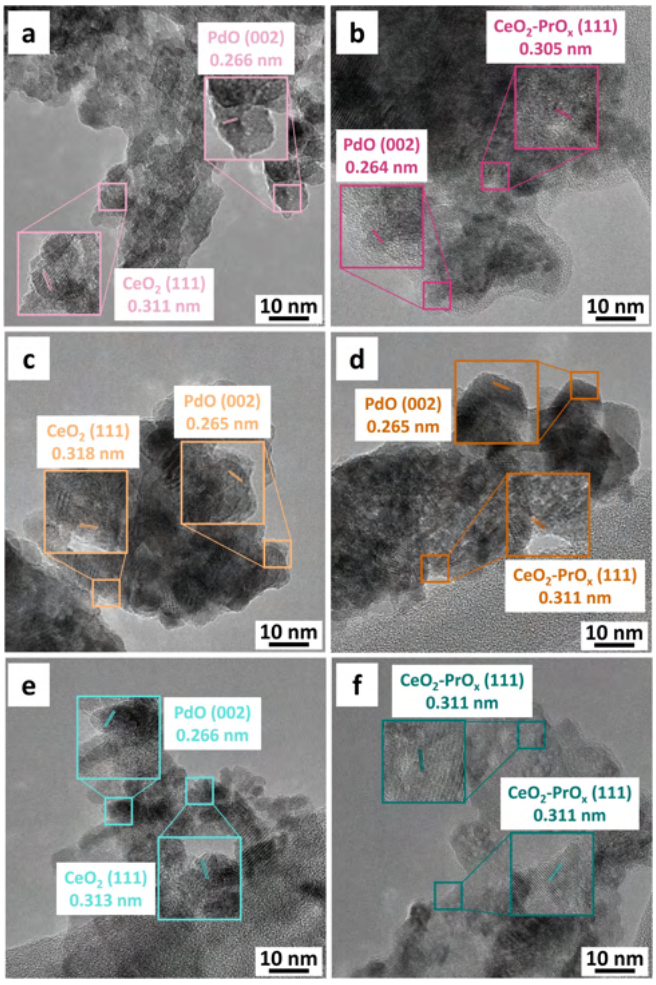

Figure 4. HRTEM images of Pd/CeO_2_S (a), Pd/Ce90Pr10_S (b), Pd/CeO_2_D (c), Pd/Ce90Pr10_D (d), Pd/CeO_2_HT (e) and Pd/Ce90Pr10_HT (f).

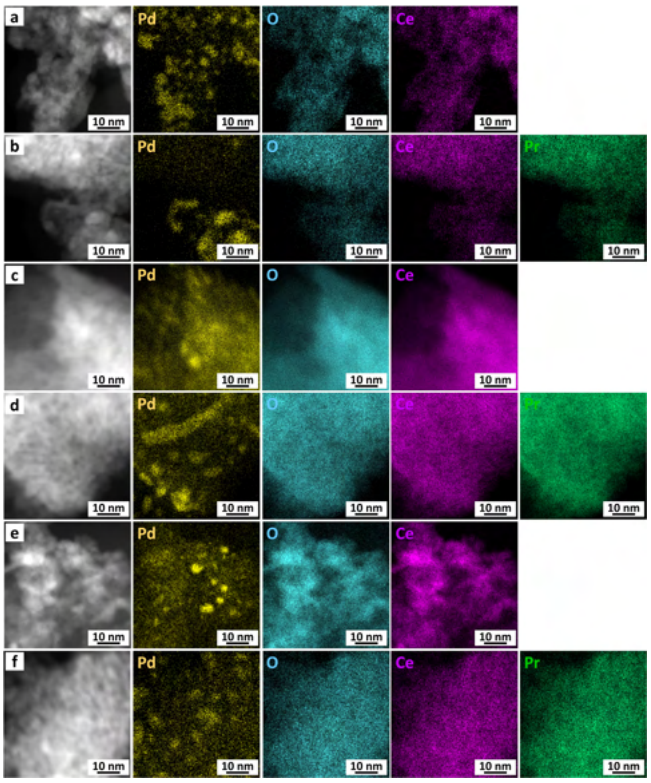

Figure 5. HAADF-STEM images and EDS maps of Pd/CeO_2_S (a), Pd/Ce90Pr10_S (b), Pd/CeO_2_D (c), Pd/Ce90Pr10_D (d), Pd/CeO_2_HT (e) and Pd/Ce90Pr10_HT (f).

Finally, high-angle annular dark-field scanning transmission electron microscopy (HAADF-STEM) investigations and corresponding energy dispersive X-ray spectroscopy (EDS) microanalysis were carried out on different regions of the catalysts. A representative area for each sample can be found in Figure 5. It is possible to note that cerium and praseodymium are uniformly distributed over the entire investigated areas. In line with XRD results, this means that segregated domains of cerium oxide and praseodymium oxide are not present within the samples and the formation of a CeO_2-PrO_x mixed phase occurred.[37] This kind of analysis was of particular relevance to examining the palladium distribution in the samples. In this respect, similar results were obtained for the materials prepared with the three synthesis methods. The noble metal was not distributed in well-defined and regular particles with homogenous size, segregated at the surface of the Ce–Pr oxide. It was rather widely spread over the catalytic supports with some irregular Pd-rich domains having an average size of 5–10 nm (Figure 5).

X-ray photoelectron spectroscopy (XPS) was performed to study the superficial oxidation state of cerium, praseodymium and palladium of the different samples. The studied regions are O 1s (Figure S4), Ce 3d (Figure S5), Pr 3d (Figure S6), and Pd 3d (Figure 6).

Spectra in the O 1s core level are visible in Figure S4. The latter were analyzed and the results coming from the deconvolution process are described in Table S2. The spectra were deconvoluted by using 3 or 4 peaks. The first contribution, localized at ~529 eV, was linked to the presence of oxygen, like the one in the crystalline framework (O^{2-}).[38] The second peak at ~531 eV and the third peak at ~534 eV can be related to either oxygen linked to Ce^{3+} ions or the presence of surface-adsorbed oxygen species (i.e. OH^- and/or CO_3^{2-} groups).[33,39–41] As to the latter, the distinction between the two contributions is quite hard to detect due to the partial overlap of the two peaks. Finally, the fourth contribution seen for Pd/Ce90Pr10_S and Pd/Ce90Pr10_D was ascribed to weakly adsorbed surface contaminations. Overall, the amount of oxygen like that of the catalyst structure (~529 eV) decreased when praseodymium was present in the materials, whereas the percentage of oxygen linked to the presence of Ce^{3+} and/or surface-adsorbed species (~534–531 eV) increased. In more detail, this change was quite slight for ceria-based spheres (S samples) and ordered mesostructures obtained with a hard template (HT samples), while a more marked difference upon Pr doping was observed for ceria dumbbells (D samples): indeed, lattice oxygen dropped from 59.3% in Pd/CeO_2_D to 38.2% in Pd/Ce90Pr10_D.

Spectra in the Ce 3d core level are shown in Figure S5. The deconvolution process was made through the use of 10 peaks

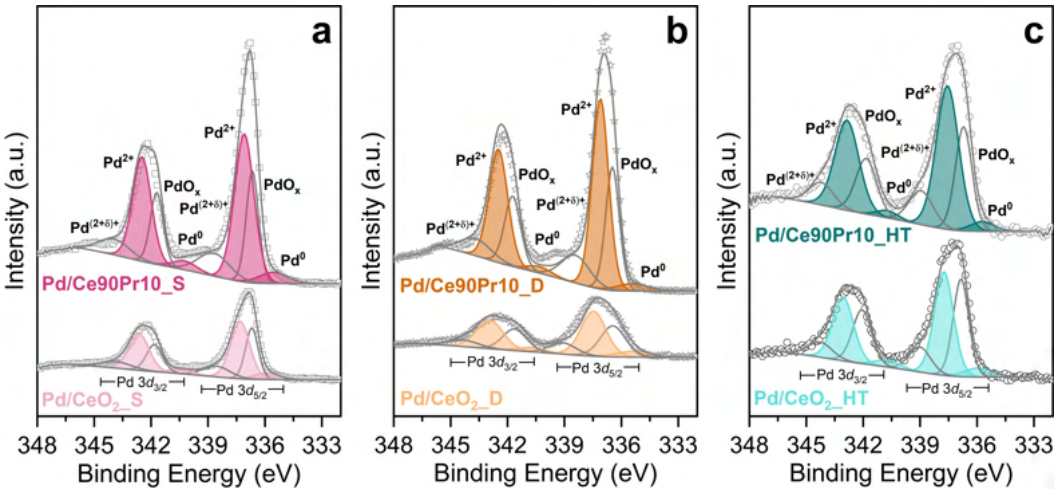

Figure 6. Deconvoluted XPS spectra in the Pd 3d core level for Pd/CeO_2_S and Pd/Ce90Pr10_S (a), Pd/CeO_2_D and Pd/Ce90Pr10_D (b), Pd/CeO_2_HT and Pd/Ce90Pr10_HT (c). Colored bands refer to Pd^{2+} and Pd^0 species.

(five for the $3d_{5/2}$ level and five for the $3d_{3/2}$ level). In particular, the v_0-u_0 and the v'-u' pairs were ascribed to the presence of Ce^{3+} ions, while the v-u, v''-u'' and v'''-u''' pairs were linked to the presence of oxidized cerium ions (Ce^{4+}).[24,34,42] Similarly, spectra in the Pr 3d core level are reported in Figure S6 and the deconvolution process was carried out with 5 peaks for the $3d_{5/2}$ level and 5 peaks for the $3d_{3/2}$ level. The b_0-a_0 and the b'-a' pairs lined to Pr^{3+} ions, while the b-a, b''-a'' and b'''-a''' pairs to Pr^{4+} ions.[43] On the whole, a mixture of oxidized and reduced Ce and Pr ions is present at the catalytic surface. The results of the deconvolution, in terms of abundance of Ce^{3+} and Pr^{3+} ions, are reported in Table 2. The amount of reduced Ce ions decreased with the introduction of praseodymium and this finding is in line with previous investigations on materials with similar composition.[15,16,43] The amount of reduced Pr ions is rather similar for the three Pd/Ce90Pr10 samples.

Spectra in the Pd 3d core level are presented in Figure 6. The deconvolution process was performed by using 8 peaks ascribed to (i) metallic Pd (Pd^0) at ~335.7 and 340.5 eV, (ii) Pd^{2+} ions linked to the presence of PdO at ~337.4 and 342.7 eV, (iii) PdO_x species characterized by an intermediate oxidation state between metallic Pd and Pd^{2+} ions at ~336.6 and 341.8 eV, and (iv) highly oxidized Pd species ($Pd^{(2+\delta)+}$) at ~338.8 and 334.0 eV.[44–46] As evident from Table 2, the percentage of reduced palladium species (Pd^0 and PdO_x) decreased with the introduction of Pr in the ceria lattice. On the other hand, the amount of more oxidized Pd compounds (Pd^{2+} and $Pd^{(2+\delta)+}$) rose with the dopant addition. It means that, in line with the previous studies,[15,16] the Pr introduction leads to the retention of palladium in a more oxidized form.

Figure 7 illustrates the reduction profiles of Pd-based catalysts between −50 and 900 °C. All the materials were characterized by a sharp peak centered around 10 °C that can be ascribed to the reduction of crystalline PdO/PdO_x species (yellow bands in Figure 7). Assuming that most Pd species are in the PdO form, their complete reduction would require a H_2 consumption of about 9.40 mmol per gram of palladium in the sample. However, the hydrogen consumption below 25 °C turned out to be lower (between 0.72 and 1.87 mmol of H_2 per g of Pd, as reported in Table 3). Thus, not all palladium is present in an isolate and crystalline form.[47,48] It stands to reason that a fraction of palladium is strictly linked to the support and consequently its reduction occurs at higher temperature. Indeed, as evident in Figure 7, it is possible to observe a substantial hydrogen consumption between 25 and 200 °C. The presence of these peaks is expected from the literature and it is commonly associated to the simultaneous reduction of palla-

Table 2. Atomic percentage of reduced Ce and Pr cations and palladium species present at the catalyst surface.

Sample	Ce^{3+}	Pr^{3+}	Pd^0	PdO_x	Pd^{2+}	$Pd^{(2+\delta)+}$
Pd/CeO_2_S	25.5	–	7.1	29.6	50.0	13.2
Pd/Ce90Pr10_S	20.4	50.3	6.0	26.0	54.3	13.7
Pd/CeO_2_D	25.0	–	7.4	32.5	47.5	12.7
Pd/Ce90Pr10_D	20.1	52.4	4.0	28.9	53.6	13.5
Pd/CeO_2_HT	24.0	–	6.0	35.4	46.1	12.5
Pd/Ce90Pr10_HT	22.1	49.1	3.9	28.8	53.8	13.6

Table 3. Specific H_2 uptake during temperature programmed reduction analysis in the −50–25 °C and 25–900 °C temperature ranges.

Sample	H_2 uptake (from −50 to 25 °C)		H_2 uptake (from 25 to 900 °C)
	$mmolH_2\,g_{Pd}^{-1}$	$mmolH_2\,g_{CAT}^{-1}$	$mmolH_2\,g_{CAT}^{-1}$
Pd/CeO_2_S	1.77	0.03	0.87
Pd/Ce90Pr10_S	1.87	0.03	1.00
Pd/CeO_2_D	1.59	0.02	0.90
Pd/Ce90Pr10_D	1.75	0.02	1.05
Pd/CeO_2_HT	0.72	0.01	0.92
Pd/Ce90Pr10_HT	0.85	0.01	0.94

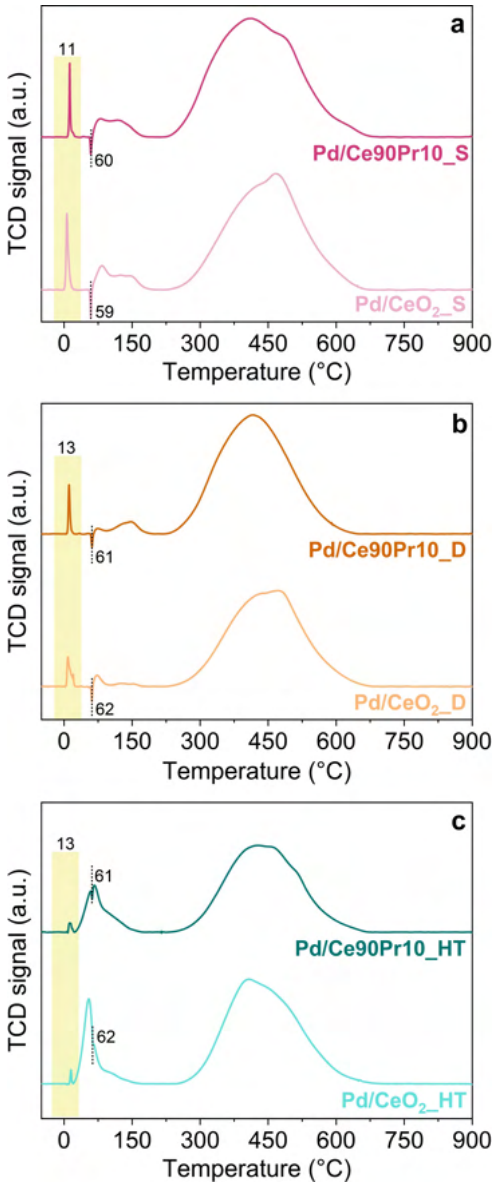

Figure 7. H_2-TPR profiles for Pd/CeO_2_S and Pd/Ce90Pr10_S (a), Pd/CeO_2_D and Pd/Ce90Pr10_D (b) and Pd/CeO_2_HT and Pd/Ce90Pr10_HT (c) from −50 to 900 °C.

dium and ceria-based support.[49] Considering the low H_2 consumption between −50 and 25 °C in Table 3 and the presence of intense peaks at 25–200 °C, this phenomenon seemed to be emphasized in the samples obtained using SBA-15 as a hard template. This means that a different synthesis method and, therefore, a different morphology could partially affect the palladium-support interactions. The negative peaks observed for all the samples at approximately 60 °C (marked with dashed lines in Figure 7) were ascribed to the decomposition of β-hydride palladium species.[50,51]

A large peak between 200 and 700 °C was detected in the reduction profiles in Figure 7 and it can be linked to the reduction of CeO_2 and Ce90Pr10 supports. In this regard, it is worth pointing out that the reduction of pure cerium oxide normally consists of two different peaks centered at 300–400 and 600–900 °C. The latter ones can be ascribed to the reduction of surface and bulk cerium species, respectively. This behavior is not present in this work and this fact is expected from previous studies.[16,49] The reduction of cerium oxide can be severely modified by the presence of palladium. Indeed, a part of CeO_2-based supports can be reduced in the 25–200 °C temperature range when palladium is present.[49]

Finally, for all the three set of samples, the overall hydrogen consumption of the Pd/Ce90Pr10 catalyst was slightly higher than that of the corresponding Pd/CeO_2 material. This fact is expected as the substitution of Ce by Pr enhances the oxygen storage capacity and the reducibility of the samples.[52]

Catalytic activity of the powdered catalysts

Figure 8 provides the methane conversion curves for the three sets of samples (Pd/CeO_2_S and Pd/Ce90Pr10_S in Figure 8a, Pd/CeO_2_D and Pd/Ce90Pr10_D in Figure 8b and Pd/CeO_2_HT and Pd/Ce90Pr10_HT in Figure 8c) in dry conditions, i.e. in the absence of water in the incoming flow. In all three cases, Pd/CeO_2 performed roughly equal to Pd/Ce90Pr10 in the 100–500 °C temperature range (see reaction rates in Table 4). Also, the catalytic activity of all the catalysts appeared almost identical (Figure S7), independently of the synthesis technique.

Overall, the activity of these new materials in the low temperature range (100–500 °C) turned out to be remarkably higher than that observed for analogous catalysts previously synthesized,[15,16] with the same chemical composition but much lower specific surface area (4–6 $m^2 g^{-1}$). For the sake of comparison, the light-off curves of Pd/Ce–Pr_D materials and those reported in[16] are displayed in Figure S8. This means that a greater surface area and a lower calcination temperature led to the obtainment of significantly more active catalysts. This phenomenon did not allow to elucidate the advantages derived from the introduction of praseodymium into the system. However, the role of Pr-doping in the low temperature range will become clearer in the CH_4 oxidation tests performed in wet conditions.

As far as the high temperature range is concerned (i.e. 500–900 °C), the dopant addition turned out to be essential to limit the typical loss of activity of Pd-based materials around 700–800 °C.[11,16] In order to investigate this aspect, two of the high-surface area materials of this work (Pd/CeO_2_D e Pd/Ce90Pr10_

Table 4. Methane oxidation reaction rates of the catalysts at 275 °C in dry conditions and at 325 °C in wet conditions.

Sample	Reaction Rates ($\mu mol_{CH4} g_{Pd}^{-1} s^{-1}$)	
	Dry @ 275 °C	Wet @ 325 °C
Pd/CeO_2_S	27.4	9.4
Pd/Ce90Pr10_S	32.2	19.4
Pd/CeO_2_D	24.7	7.9
Pd/Ce90Pr10_D	33.9	19.1
Pd/CeO_2_HT	41.1	17.2
Pd/Ce90Pr10_HT	33.4	17.4

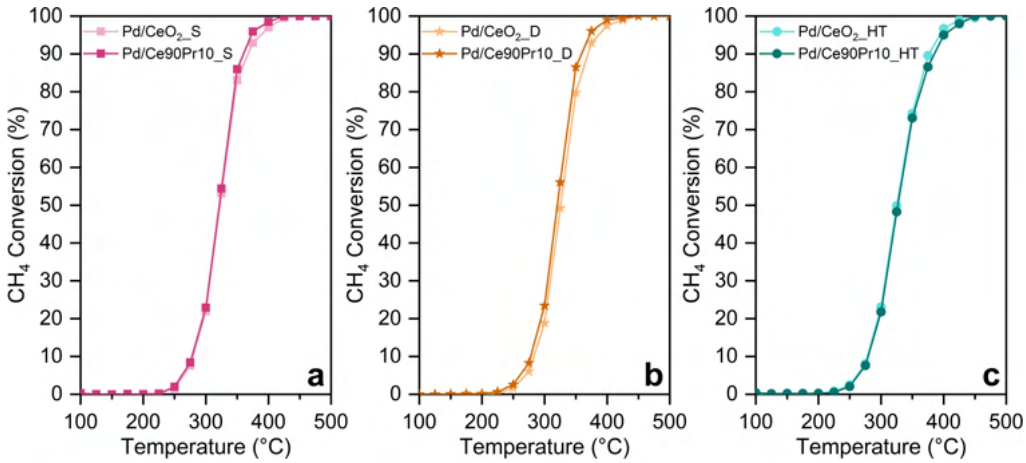

Figure 8. CH_4 oxidation light-off curves for Pd/CeO_2_S and Pd/Ce90Pr10_S (a), Pd/CeO_2_D and Pd/Ce90Pr10_D (b), Pd/CeO_2_HT and Pd/Ce90Pr10_HT (c) in dry conditions. The first heating cycle is reported.

D) were tested up to 900 °C. More specifically, one heating run up to 500 °C was performed, followed by cooling and by another heating ramp up to 900 °C (cycle 1 in Figure 9a and cycle 2 in Figure 9b). Overall, the Pr role was confirmed by carrying out these tests. Indeed, looking at the second cooling run (dashed lines in Figure 9b), the loss of activity at about 700–750 °C was significantly reduced in the presence of Pr. In compliance with previous studies,[15,16] this phenomenon is due to the strong interactions between palladium and praseodymium oxides. The latter, at a high enough temperature, can lead to the formation of a PdO-PrO_x mixed phase which has proved to be stable up to 1200 °C.[53]

Finally, focusing on the cooling runs in Figure 9b, it is possible to notice that their activity is markedly lower than that of the heating runs reported in the same figure. This is due to the fact that these materials were calcined at 500 °C, and thus they are not appropriate for operating at higher temperatures. In fact, heating these materials up to 900 °C led to a substantial decrease in their surface area (data in Table S3). This kind of tests was only performed to investigate and confirm the role of praseodymium at high temperature. Considering that these materials were calcined at 500 °C, it is clear that they can only be used up to 500 °C in practical applications.

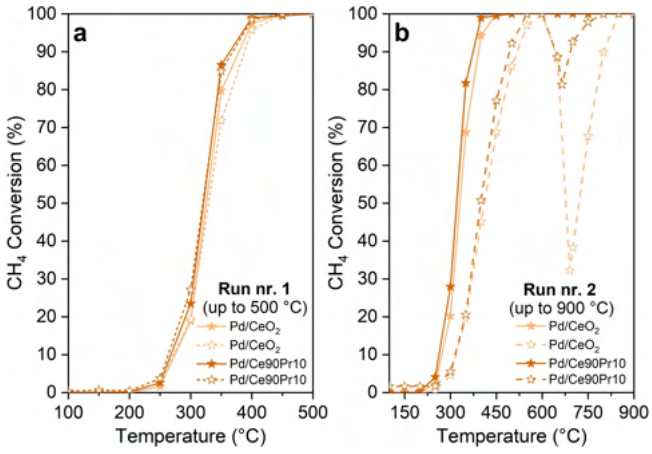

Figure 9. CH_4 oxidation light-off curves for Pd/CeO_2_D and Pd/Ce90Pr10_D in dry conditions during the first heating run up to 500 °C (a) and during the second heating run up to 900 °C (b). Solid lines refer to the heating runs while dashed lines refer to the cooling runs.

On the whole, in the low temperature range (100–500 °C) the palladium deposition on ceria and ceria-praseodymia samples with high surface area leads to the preparation of materials with better activity compared to that obtained in previous studies concerning similar catalysts with lower SSA.[15,16] Furthermore, the role of praseodymium was confirmed by carrying out a second heating cycle up to 900 °C. The presence of a low percentage of dopant was indeed able to provide thermal stability to the system by markedly reducing the high-temperature loss of activity due to the PdO–Pd transition.

Figure 10 reports the methane conversion curves in wet conditions, i.e. when water is added to the inlet flow. As well known, the presence of water plays a detrimental role for palladium-based catalysts.[14,54,55] Indeed, water adsorbs on the surface of PdO clusters with the formation of hydroxyl species and their presence blocks the active sites necessary for methane adsorption and activation. Comparing Figures 8 and 10, this effect was confirmed also for the catalysts of the present study. A loss in performance was observed by introducing water into the system. However, considering Figure 10 and Table 4, it appears that the presence of praseodymium played a beneficial role for all the three systems. All the Pd/Ce90Pr10 samples showed indeed higher activity than Pd/CeO_2 samples in the presence of H_2O. This outcome strongly confirms the activity trend observed in previous studies[15,16] and can be related to the higher affinity of Pd/Ce90Pr10 with hydrocarbons than water, reported in.[16]

Figures 8 and 10 illustrate the performance of the materials for the CH_4 oxidation reaction during the first heating run. It is necessary, however, to investigate whether this activity level is maintained for several hours during the reaction. In this regard, the long-term stability of a pair of synthesized materials (Pd/

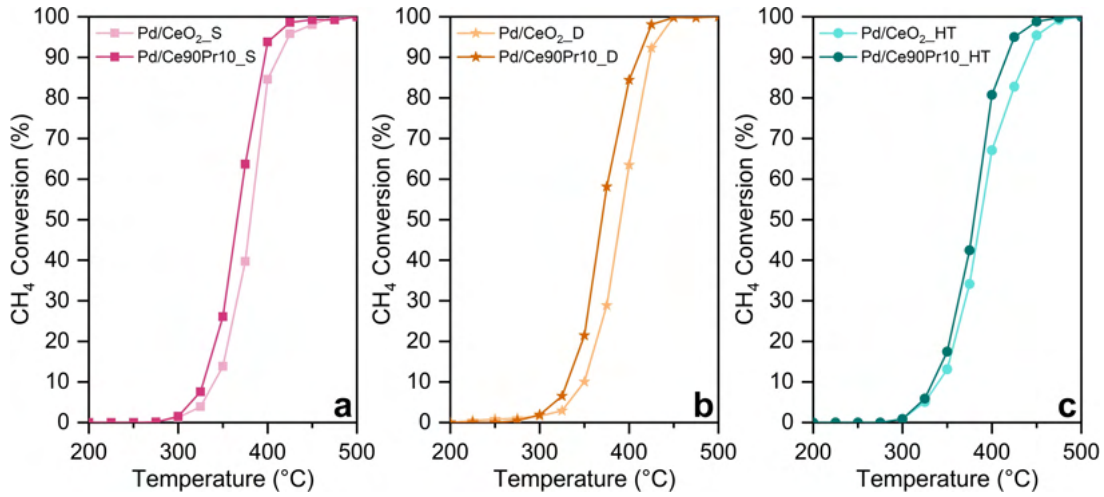

Figure 10. CH_4 oxidation light-off curves for Pd/CeO_2_S and Pd/Ce90Pr10_S (a), Pd/CeO_2_D and Pd/Ce90Pr10_D (b), Pd/CeO_2_HT and Pd/Ce90Pr10_HT (c) in wet conditions. The first heating cycle is reported

CeO_2_HT and Pd/Ce90Pr10_HT) was studied by blocking the first heating curve at 420 °C (temperature equivalent to 85% conversion for Pd/CeO2_HT and 90% conversion for Pd/Ce90Pr10_HT). Then, the samples were exposed to the reaction mixture for 6 hours. As displayed in Figure 11, both materials achieved good results during these stability tests and no loss of performances was observed throughout the six hours investigated. Additionally, it is interesting to note that Pd/Ce90Pr10_HT sample showed a significantly higher activity compared to Pd/CeO_2_HT. This finding strongly confirms the beneficial role of Pr, especially during wet methane oxidation experiments.

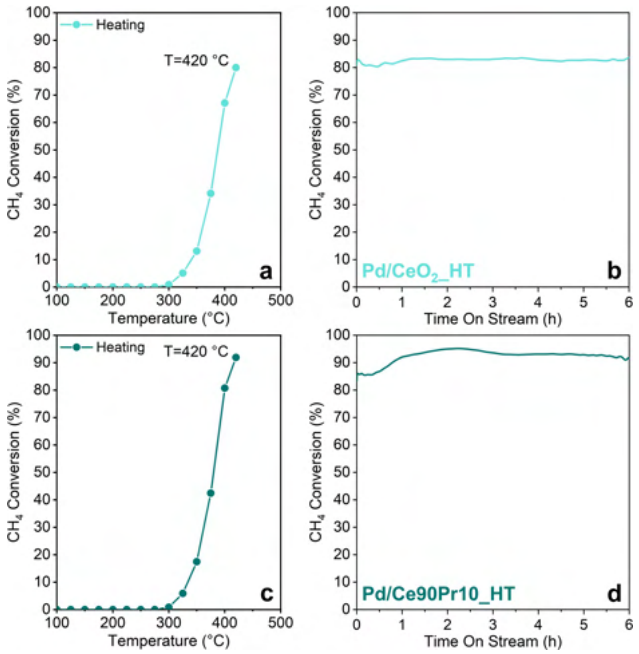

Figure 11. Results of the long-term stability tests performed during methane oxidation in wet conditions for Pd/CeO_2_HT (a,b) and Pd/Ce90Pr10_HT (c,d).

Conclusions

In this work CeO_2 and Ce90Pr10 supports with high surface area were prepared with three different techniques (i.e. employing a microwave device, with a hydrothermal synthesis and through the use of SBA-15 as a hard template). Then, the catalytic carriers were impregnated with palladium and calcined at 500 °C.

All the materials exhibited very similar features according to the employed characterization techniques in the temperature range between room temperature and 500 °C. Considering the catalytic activity in dry conditions, these samples outperformed previously studied materials having the same composition but a lower surface area. Therefore, these results provide compelling evidence of an increase in the performance of the Pd/Ce–Pr system compared to previous studies. The role of praseodymium in dry conditions was confirmed by lengthening the tests up to 900 °C. Indeed, in the high-temperature range, the role of the dopant was pivotal to significantly reducing the high-temperature loss of activity of Pd-based catalysts. The importance of praseodymium was also revealed in the wet methane conversion curves. As a matter of fact, all the Pd/Ce90Pr10 catalysts showed better performances in the presence of water. Finally, although both Pd/CeO_2 and Pd/Ce90Pr10 samples were distinguished by great stability under reaction conditions during the long-term experiments, the presence of Pr was essential to maintain a higher conversion.

All in all, this study provides compelling evidence that the introduction of 10% of Pr into the ceria lattice is beneficial for both the low-temperature activity and the high-temperature stability of supported Pd-based catalysts, clearly demonstrating the advantages of using such mixed systems.

Experimental Section

Catalyst synthesis

High surface area CeO_2 and Ce90Pr10 materials (Ce–Pr mixed oxide with molar Ce-to-Pr ratio of 9) were synthesized according to three different preparation methods adapted from procedures previously reported in the literature.

CeO_2 and Ce90Pr10 spheres (CeO2_S and Ce90Pr10_S samples):[29] $Ce(NO_3)_3 \cdot 6H_2O$ (99.99%, Sigma-Aldrich) and $Pr(NO_3)_3 \cdot 6H_2O$ (99.99%, Sigma-Aldrich) were dissolved in distilled water to obtain a 0.1 M nitrate solution. 3.6 g of urea was added to obtain a urea-to-final oxide molar ratio equal to 4. Then, the obtained solution was treated in an Anton Paar Multiwave 5000 microwave digestion apparatus at 120 °C for 1 h (ramp of 30 °C min^{-1}). Lastly, the precipitated solid was washed and recovered through centrifugation (4500 rpm, 5 min), dried overnight at 50 °C and calcined at 500 °C for 2 h (ramp of 5 °C min^{-1}).

CeO_2 and Ce90Pr10 dumbbells (CeO2_D and Ce90Pr10_D samples):[30] $Ce(NO_3)_3 \cdot 6H_2O$ (99.99%, Sigma-Aldrich) and $Pr(NO_3)_3 \cdot 6H_2O$ (99.99%, Sigma-Aldrich) were dissolved in distilled water to obtain a 0.1 M nitrate solution. 1.8 g of urea was added to obtain a urea-to-final oxide molar ratio equal to 2. The solution was treated in a stainless-steel autoclave with an inner Teflon liner at 120 °C for 8 h. The obtained solid was washed and recovered by centrifugation (4500 rpm, 5 min). After a drying process at 80 °C for 4 h, the oxides were calcined at 500 °C for 2 h (ramp of 5 °C min^{-1}).

CeO_2 and Ce90Pr10 with hard template method (CeO_2_HT and Ce90Pr10_HT samples):[31] a total amount of 0.0175 mol of $Ce(NO_3)_3 \cdot 6H_2O$ (99.99%, Sigma-Aldrich) and $Pr(NO_3)_3 \cdot 6H_2O$ (99.99%, Sigma-Aldrich) was dissolved in 25 mL of ethanol. 1 g of SBA-15 was added to 15 mL of the obtained solution and the system was stirred for 1 h at RT. Then, the solvent was removed by evaporation at 60 °C by using a heating plate. Once the solvent was removed, the impregnation process was repeated to completely fill the pores of the SBA-15 template. The obtained solid was calcined at 500 °C for 2 h (ramp of 5 °C min^{-1}). The SBA-15 template was removed by treating the solid with a NaOH solution (2 M) at 50 °C. The Ce–Pr supports were then washed until they reached a pH equal to 7, dried at 60 °C overnight and calcined at 500 °C for 2 h (ramp of 5 °C min^{-1}).

Pd was deposited on these supports through incipient wetness impregnation. In particular, 1.5 g of each support was treated with a $Pd(NO_3)_2$ solution and subsequently calcined at 500 °C for 1 h (ramp of 5 °C min^{-1}) to obtain 2 wt% of Pd in the final oxide.

Catalyst characterization

The specific surface areas of the synthesized materials were estimated via nitrogen physisorption at −196 °C, performed in a Micromeritics Tristar II 3020, by using the Brunauer-Emmett-Teller (BET) algorithm. Pore volume was measured in the last point of the adsorption isotherm ($p/p^0 = 0.98$). Prior to the analysis, the catalyst powder underwent a cleaning pretreatment at 200 °C for 2 h in a nitrogen stream.

Powder X-ray diffraction (XRD) analysis was conducted using a Philips X'Pert PW3040 diffractometer. The patterns were collected in a 2θ angle range from 20 to 80° by using Cu Kα radiation with a wavelength of 1.5419 Å. The average crystallite dimension was calculated with the Debye-Scherrer formula, assuming a shape factor equal to 0.9 and correcting the instrumental peak broadening using a lanthanum hexaboride (LaB_6) crystal as a standard reference.

The chemical composition of the catalysts, in terms of Ce/Pr ratio and Pd loading, was verified via inductively coupled plasma-mass spectrometry (ICP-MS) with a Thermo Scientific iCAP RQ ICP-MS. The mixed oxides were dissolved in an aqueous solution of nitric acid, hydrochloric acid, and hydrogen peroxide, performing a heat treatment at 200 °C for 30 min.

Field emission scanning electron microscopy (FESEM) was performed to investigate the catalyst morphology, using a Zeiss Merlin microscope with a Gemini-II column. The solid powder was spread on conductive carbon tape and coated with a 5-nm-thick Pt layer through sputter deposition, to improve the quality of images.

High-resolution transmission electron microscopy (HRTEM) images were obtained using a Thermo Scientific Talos F200X microscope operating at 200 kV. The sample powder was deposited on a copper grid by drop-casting a suspension of catalyst powder in 2-propanol. With the same apparatus, elemental distribution was observed by acquiring energy dispersive X-ray spectroscopy (EDS) maps in high-angle annular dark-field scanning-transmission electron microscopy mode (HAADF-STEM).

X-ray photoelectron spectroscopy (XPS) was employed to study the surface chemistry of the catalysts and the oxidation states of Ce, Pr and Pd. XPS measurements were performed in a PHI 5000 Versa Probe instrument with a monochromatic Al Kα X-ray source (1486.6 eV). High-resolution spectra were acquired using a band-pass energy of 23.50 eV, a take-off angle of 45°, and an X-ray spot diameter of 100.0 μm. Surface charging effects were compensated by referencing the C 1s peak at 284.8 eV. Casa XPS software (version 2.3.16) was used for data analysis.

Temperature programmed reduction with hydrogen (H_2-TPR) was performed to investigate the catalyst reducibility, by employing an Altamira Ami-300Lite instrument supplied with a thermal conductivity detector (TCD). The sample powder (50 mg) was placed in a U-tube reactor with an internal thermocouple, and it was pre-treated in O_2 (30 mL min^{-1}) at 300 °C for 30 min. The reactor was then purged with pure He, cooled down to room temperature, and inserted in a 2-propanol/liquid nitrogen bath to keep the temperature around −70 °C. Reduction was carried out in a 25 mL min^{-1} flow of 5 vol% H_2 in Ar, heating the reactor with a 10 °C min^{-1} ramp from −50 to 900 °C.

Catalytic activity tests

The catalytic activity towards methane oxidation was assessed by performing experiments in a quartz U-tube reactor with a 4 mm inner diameter, placed in a PID-controlled furnace. The catalytic bed, containing 50 mg of catalyst powder mixed with 150 mg of silicon carbide to avoid local hot spots, was supported on a quartz wool bed. A thermocouple was inserted just above the powder bed, to monitor the temperature within the reactor.

After a pretreatment in air flow at 100 °C for 30 min, a gaseous mixture containing 0.3 vol% CH_4 and 1.2 vol% O_2 in N_2 was sent to the reactor. During tests in wet conditions, 5 vol% water was added to the inlet stream, thanks to a Bronkhorst Controlled Evaporation and Mixing (CEM) system. In any case, a total flow rate of 150 mL min^{-1} was used, corresponding to a gas hourly space velocity (GHSV) between 60,000 and 80,000 h^{-1}, depending on the bulk density of the catalyst. The concentrations of CH_4, CO, CO_2, and O_2 at the reactor outlet were monitored with an ABB AO2020 non-dispersive infrared analyzer and an Emerson XStream X2GP paramagnetic analyzer.

During each test, the catalyst bed was heated up to 500 °C ad then cooled down to 100 °C, with a 5 °C min^{-1} rate. A second heating and

cooling cycle, equal to the first one, was then carried out, verifying that the catalyst performance remained unchanged after the first cycle. Additional tests at higher temperatures were performed by heating the reactor up to 900 °C during the second cycle. Finally, the stability of the catalysts was assessed through long runs in wet conditions, exposing the samples to the reaction mixture at 420 °C for 6 h.

Acknowledgements

The authors greatly thank Shaila Femia for helping in data collection during her MS thesis preparation. Camilla Galletti and Marco Allione are kindly acknowledged as well for performing XRD, FESEM and TEM analyses. The authors acknowledge the funding received by the Italian Ministero dell'Università e della Ricerca (MUR) under the Dipartimento di Eccellenza 2018–2022 program and the PON Ricerca e Innovazione "REACT-EU" project (DM 1062/21).

Conflict of Interests

The authors declare no conflict of interest.

Data Availability Statement

The data that support the findings of this study are available from the corresponding author upon reasonable request.

Keywords: Methane oxidation · Pd-ceria catalysts · Praseodymium · High surface area · Water-induced deactivation

[1] D. Jiang, K. Khivantsev, Y. Wang, *ACS Catal.* **2020**, *10*, 14304–14314.
[2] P. Divekar, X. Han, X. Zhang, M. Zheng, J. Tjong, *Energy.* **2023**, *263*, 125769.
[3] R. B. Jackson, M. Saunois, P. Bousquet, J. G. Canadell, B. Poulter, A. R. Stavert, P. Bergamaschi, Y. Niwa, A. Segers, A. Tsuruta, *Environ. Res. Lett.* **2020**, *15*, 071002.
[4] L. Feng, P. I. Palmer, R. J. Parker, M. F. Lunt, H. Bösch, *Atmos. Chem. Phys.* **2023**, *23*, 4863–4880.
[5] R. B. Skeie, Ø. Hodnebrog, G. Myhre, *Commun. Earth Environ.* **2023**, *4*, 1–14.
[6] E. D. Goodman, A. A. Ye, A. Aitbekova, O. Mueller, A. R. Riscoe, T. Nguyen Taylor, A. S. Hoffman, A. Boubnov, K. C. Bustillo, M. Nachtegaal, S. R. Bare, M. Cargnello, *J. Chem. Phys.* **2019**, *151*, 154703.
[7] J. J. Willis, A. Gallo, D. Sokaras, H. Aljama, S. H. Nowak, E. D. Goodman, L. Wu, C. J. Tassone, T. F. Jaramillo, F. Abild-Pedersen, M. Cargnello, *ACS Catal.* **2017**, *7*, 7810–7821.
[8] M. Danielis, N. J. Divins, J. Llorca, L. Soler, X. Garcia, I. Serrano, L. E. Betancourt, W. Xu, J. A. Rodríguez, S. D. Senanayake, S. Colussi, A. Trovarelli, *EES Catal.* **2023**, *1*, 144–152.
[9] M. Giuliano, M. C. Valsania, P. Ticali, E. Sartoretti, S. Morandi, S. Bensaid, G. Ricchiardi, M. Sgroi, *Catalysts.* **2021**, *11*, 1–15.
[10] W. Yang, M. Y. Kim, F. Polo-Garzon, J. Gong, X. Jiang, Z. Huang, M. Chi, X. Yu, X. Wang, Y. Guo, Z. Wu, *Chem. Eng. J.* **2023**, *451*, 138930.
[11] S. Colussi, P. Fornasiero, A. Trovarelli, *Chinese J. Catal.* **2020**, *41*, 938–950.
[12] P. Velin, M. Ek, M. Skoglundh, A. Schaefer, A. Raj, D. Thompsett, G. Smedler, P. A. Carlsson, *J. Phys. Chem. C.* **2019**, *123*, 25724–25737.
[13] M. Monai, T. Montini, C. Chen, E. Fonda, R. J. Gorte, P. Fornasiero, *ChemCatChem.* **2015**, *7*, 2038–2046.
[14] K. Keller, P. Lott, S. Tischer, M. Casapu, J. D. Grunwaldt, O. Deutschmann, *ChemCatChem.* **2023**, *15*, 1–11.
[15] S. Ballauri, E. Sartoretti, C. Novara, F. Giorgis, M. Piumetti, D. Fino, N. Russo, S. Bensaid, *Catal. Today.* **2022**, *390–391*, 185–197.
[16] S. Ballauri, E. Sartoretti, M. Hu, C. D'Agostino, Z. Ge, L. Wu, C. Novara, F. Giorgis, M. Piumetti, D. Fino, N. Russo, S. Bensaid, *Appl. Catal. B Environ.* **2023**, *320*, 121898.
[17] L. Wu, W. Fan, X. Wang, H. Lin, J. Tao, Y. Liu, J. Deng, L. Jing, H. Dai, *Catalysts.* **2023**, *13*, 1–25.
[18] R. L. Mortensen, H. D. Noack, K. Pedersen, S. Mossin, J. Mielby, *ChemCatChem.* **2022**, *14*, 1–16.
[19] S. Abdollahzadeh-Ghom, C. Zamani, T. Andreu, M. Epifani, J. R. Morante, *Appl. Catal. B Environ.* **2011**, *108–109*, 32–38.
[20] E. Rombi, M. G. Cutrufello, L. Atzori, R. Monaci, A. Ardu, D. Gazzoli, P. Deiana, I. Ferino, *Appl. Catal. A Gen.* **2016**, *515*, 144–153.
[21] M. Thommes, K. Kaneko, A. V. Neimark, J. P. Olivier, F. Rodriguez-Reinoso, J. Rouquerol, K. S. W. Sing, *Pure Appl. Chem.* **2015**, *87*, 1051–1069.
[22] M. M. Ravindra, R. Shirasangi, H. P. Dasari, M. B. Saidutta, *Appl. Surf. Sci. Adv.* **2023**, *16*, 100413.
[23] M. Dosa, M. J. Marin-figueredo, E. Sartoretti, C. Novara, F. Giorgis, S. Bensaid, D. Fino, N. Russo, M. Piumetti, *Catalysts.* **2022**, *12*, 1–23.
[24] F. Salomone, E. Sartoretti, S. Ballauri, M. Castellino, C. Novara, F. Giorgis, R. Pirone, S. Bensaid, *Catal. Today.* **2023**, *423*, 114023.
[25] E. Sartoretti, C. Novara, A. Chiodoni, F. Giorgis, M. Piumetti, S. Bensaid, N. Russo, D. Fino, *Catal. Today.* **2022**, *390–391*, 117–134.
[26] R. D. Shannon, *Acta Cryst.* **1976**, *32*, 751–767.
[27] M. Danielis, J. D. Jiménez, N. Rui, J. Moncada, L. E. Betancourt, A. Trovarelli, J. A. Rodriguez, S. D. Senanayake, S. Colussi, *Appl. Catal. A Gen.* **2023**, *660*, 119185.
[28] E. Poggio-Fraccari, B. Irigoyen, G. Baronetti, F. Mariño, *Appl. Catal. A Gen.* **2014**, *485*, 123–132.
[29] R. O. Fuentes, L. M. Acuña, A. G. Leyva, R. T. Baker, H. Pan, X. Chen, J. J. Delgado-Jaén, *J. Mater. Chem. A.* **2018**, *6*, 7488–7499.
[30] R. Suarez Anzorena, F. F. Muñoz, P. Bonelli, A. L. Cukierman, S. A. Larrondo, *Ceram. Int.* **2020**, *46*, 11776–11785.
[31] A. Lolli, R. Amadori, C. Lucarelli, M. G. Cutrufello, E. Rombi, F. Cavani, S. Albonetti, *Microporous Mesoporous Mater.* **2016**, *226*, 466–475.
[32] M. Piumetti, T. Andana, S. Bensaid, N. Russo, D. Fino, R. Pirone, *Nanoscale Res. Lett.* **2016**, *11*, 165.
[33] J. Shi, H. Li, A. Genest, W. Zhao, Q. Pengfei, T. Wang, G. Rupprechter, *Appl. Catal. B Environ.* **2022**, *301*, 120789.
[34] E. Sartoretti, C. Novara, M. C. Paganini, M. Chiesa, M. Castellino, F. Giorgis, M. Piumetti, S. Bensaid, D. Fino, N. Russo, *Catal. Today.* **2023**, *420*, 114037.
[35] B. M. Reddy, G. Thrimurthulu, L. Katta, Y. Yamada, S. E. Park, *J. Phys. Chem. C.* **2009**, *113*, 15882–15890.
[36] J. Jiang, C. Wang, S. Zhao, F. Xue, L. Li, M. Cui, X. Qiao, Z. Fei, *J. Environ. Chem. Eng.* **2023**, *11*, 109825.
[37] Y. Ding, Y. Jia, M. Jiang, Y. Guo, Y. Guo, L. Wang, Q. Ke, M. Ngoc, S. Dai, W. Zhan, *Chem. Eng. J.* **2021**, *416*, 129150.
[38] Z. Mei, Y. Li, M. Fan, L. Zhao, J. Zhao, *Chem. Eng. J.* **2015**, *259*, 293–302.
[39] C. Barth, C. Laffon, R. Olbrich, A. Ranguis, P. Parent, M. Reichling, *Sci. Rep.* **2016**, *6*, 2–7.
[40] X. Garcia, L. Soler, N. J. Divins, X. Vendrell, I. Serrano, I. Lucentini, J. Prat, E. Solano, M. Tallarida, C. Escudero, J. Llorca, *Catalysts.* **2020**, *10*, 1–48.
[41] T. Hasegawa, S. M. F. Shahed, Y. Sainoo, A. Beniya, N. Isomura, Y. Watanabe, T. Komeda, *J. Chem. Phys.* **2014**, *140*, 044711.
[42] T. Andana, K. G. Rappé, N. C. Nelson, F. Gao, Y. Wang, *Appl. Catal. B Environ.* **2022**, *316*, 121522.
[43] E. Poggio-Fraccari, G. Baronetti, F. Mariño, *J. Electron Spectros. Relat. Phenomena.* **2018**, *222*, 1–4.
[44] S. Colussi, A. Gayen, M. Boaro, J. Llorca, A. Trovarelli, *ChemCatChem.* **2015**, *7*, 2222–2229.
[45] L. S. Kibis, A. I. Stadnichenko, S. V. Koscheev, V. I. Zaikovskii, A. I. Boronin, *J. Phys. Chem. C.* **2012**, *116*, 19342–19348.
[46] R. V. Gulyaev, A. I. Stadnichenko, E. M. Slavinskaya, A. S. Ivanova, S. V. Koscheev, A. I. Boronin, *Appl. Catal. A Gen.* **2012**, *439–440*, 41–50.
[47] V. Ferrer, A. Moronta, J. Sanchez, R. Solano, S. Bernal, D. Finol, *Catal. Today.* **2005**, *108*, 487–492.
[48] A. Toso, S. Colussi, S. Padigapaty, C. de Leitenburg, A. Trovarelli, *Appl. Catal. B Environ.* **2018**, *230*, 237–245.
[49] D. Kaya, D. Singh, S. Kincal, D. Uner, *Catal. Today.* **2019**, *323*, 141–147.
[50] M. Boudart, H. S. Hwang, *J. Catal.* **1975**, *39*, 44–52.

[51] T. Fovanna, M. Nachtegaal, A. H. Clark, O. Kröcher, D. Ferri, *ACS Catal.* **2023**, *13*, 3323–3332.
[52] Z. Song, W. Liu, H. Nishiguchi, A. Takami, K. Nagaoka, Y. Takita, *Appl. Catal. A Gen.* **2007**, *329*, 86–92.
[53] T. C. Chou, T. Kennelly, R. J. Farrauto, US Patent 5 169 300: Praseodymium-palladium binary oxide, catalyst, methods of combustion and regeneration, **1992**.
[54] X. Li, X. Wang, K. Roy, J. A. Van Bokhoven, L. Artiglia, *ACS Catal.* **2020**, *10*, 5783–5792.
[55] P. Velin, F. Hemmingsson, A. Schaefer, M. Skoglundh, K. A. Lomachenko, A. Raj, D. Thompsett, G. Smedler, P. A. Carlsson, *ChemCatChem.* **2021**, *13*, 3765–3771.

Manuscript received: October 25, 2023
Revised manuscript received: December 16, 2023
Version of record online: ■■, ■■

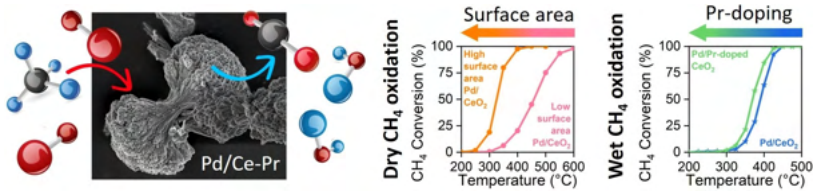

High-surface-area materials consisting of pure and Pr-doped ceria were synthesized with different procedures and employed as supports for Pd-based catalysts. Thanks to their peculiar textural properties and better Pd dispersion, these mixed oxides exhibited remarkably higher activity towards methane oxidation with respect to analogous samples with low surface area. Pr-doping resulted particularly beneficial in wet conditions, reducing water-induced deactivation effects.

S. Ballauri, Dr. E. Sartoretti, Dr. M. Castellino, Prof. M. Armandi, Prof. M. Piumetti, Prof. D. Fino, Prof. N. Russo, Prof. S. Bensaid**

1 – 12

Mesoporous Ceria and Ceria-Praseodymia as High Surface Area Supports for Pd-based Catalysts with Enhanced Methane Oxidation Activity